Self-Stabilized 50 Gb/s Silicon Photonic Microring Modulator Using a Power-Independent and Calibration-Free Control Loop

Vittorio Grimaldi, Francesco Zanetto, Fabio Toso, Ioannis Roumpos, Themistoklis Chrysostomidis, Alessandro Perino, Matteo Petrini, Francesco Morichetti, Andrea Melloni, Nikos Pleros, Miltiadis Moralis-Pegios, Konstantinos Vyrsokinos, Giorgio Ferrari and Marco Sampietro

***Abstract*—This paper demonstrates the possibility of automatically stabilizing the working condition of an integrated Silicon Photonics microring modulator with a novel dithering-based control scheme. The proposed feedback strategy leverages a real-time acquisition of the modulator non-linear transfer function (TF) and operates by setting the target locking point to the zero of the TF second derivative, i.e. where the ring slope is maximum. This results in a control algorithm that is both power-independent and calibration-free. The paper shows that the operating point identified in this way has a negligible difference with respect to the optimum working condition of minimum Transmitter Penalty normally targeted and that the employed dithering signal does not affect the modulation quality. The control performances, made possible by an FPGA-based platform ensuring a 30 ms response time, are assessed in a 50 Gbit/s routing scenario, demonstrating effective compensation of wavelength and thermal variations and successful transmission even in demanding environments.**

***Index Terms*—Silicon photonics, optical transmitter, microring modulator, thermal drift compensation, closed-loop control.**

I. Introduction

The ever-increasing demand for data traffic and bandwidth [1] has sparked an interest in integrated photonic technologies, with the ambition of replacing traditional electronic links with low-loss high-bandwidth optical interconnections [2]–[6]. Silicon Photonics is well positioned to satisfy these requirements, since it can leverage the solid know-how of the CMOS industry to achieve scalable costs and dimensions [7], [8]. Electro-optical transmitters, in particular, significantly benefit of the small curvature radius that can be achieved in Silicon Photonics, allowing to realize microring modulators (MRM) with very high Q-factors and compact footprint [9]. These features translate into high modulation efficiencies and low driving voltages, since a small shift of the MRM transfer function is needed to produce a significant light variation at the output. MRMs are therefore advantageous in terms of area and dynamic operating power over other kinds of modulators, like Mach-Zehnder-based structures [10], [11].

Despite these advantages, the diffusion of MRMs in Silicon Photonics is impaired by their high sensitivity to temperature variations, that prevents open-loop operations in thermally-challenging environments, such as datacenters [12]–[14]. To overcome this limitation, efforts are being devoted to implement efficient closed-loop control strategies for stabilizing the modulator working point, counteracting the effect of temperature instabilities and fabrication tolerances.

Several approaches have been proposed in literature to control MRMs. In [12], an external photodetector is used to assess the working condition of the ring modulator. This information is then compared to a reference value and the difference between the two is fed to a PID controller, that drives the integrated actuator until the measured signal and the reference are equal. The problem of this approach is that any fluctuation of the input optical power changes the convergence point of the control system. In [15], [16], two photodetectors are used to measure the average power in the waveguide and the working condition of the MRM, and a custom integrated circuit is used to stabilize the device by locking the ratio of the two signals. This solution requires however a precise calibration that has to be performed for each fabricated structure, since the exact ratio is affected by fabrication mismatches. In [17], a photodiode on the drop port is used to monitor in realtime the optical modulation amplitude at the output of the MRM. Although effective, this technique requires complex high-speed electronics to counteract the effect of phenomena with a slow time evolution (usually in the milliseconds time scale) and stabilize the modulator operating condition. The power consumption of the controller thus increases with the modulation frequency and it can become a relevant contribution at high transmission rates.

In this paper, we discuss a novel solution to stabilize the working point of a Silicon microring modulator based on the dithering technique, that is both power-independent and calibration-free. It relies on the extraction of the second derivative of the MRM transfer function to stabilize its operating conditions regardless of the average optical power in the system. This solution is shown to introduce no additional losses nor any measurable degradation on the modulation

Manuscript received –; revised –.

This work was supported by EU H2020 projects NEBULA (n. 871658) and SuperPixels (n. 829116).

V. Grimaldi, F. Zanetto, F. Toso, A. Perino, M. Petrini, F. Morichetti, A. Melloni, G. Ferrari and M. Sampietro are with the Department of Electronics, Information and Bioengineering, Politecnico di Milano, 20133 Milano, Italy (e-mail: vittorio.grimaldi@polimi.it; francesco.zanetto@polimi.it; fabio.toso@polimi.it; alessandro.perino@polimi.it; matteo.petrini@polimi.it; francesco.morichetti@polimi.it; andrea.melloni@polimi.it; giorgio.ferrari@polimi.it; marco.sampietro@polimi.it).

I. Roumpos, T. Chrysostomidis, K. Vyrsokinos are with the Department of Physics; N. Pleros, M. Moralis-Pegios are with the Department of Informatics, Center for Interdisciplinary Research and Innovation, Aristotle University of Thessaloniki, 54124 Thessaloniki, Greece (e-mail: ioroumpo@auth.gr; tchrysos@auth.gr; npleros@csd.auth.gr; mmoralis@csd.auth.gr; kv@auth.gr).

quality. After discussing the second-derivative approach in Section II, Section III describes the photonic chip used for the experiments and the electronic system for the MRM control. Section IV assesses the performance of the modulator stabilized with the proposed locking strategy. Section V finally reports on $50\,\mathrm{Gbit/s}$ transmission experiments, demonstrating the effectiveness of the control scheme in compensating temperature and wavelength drifts in a practical scenario.

II. Second-Derivative-based control strategy

Figure 1 shows a schematic view of the MRM that has been used in this work. The device features a pn junction along its circumference, that acts as a high-speed electro-optic actuator and induces shifts of the resonant wavelength when its reverse bias voltage is modulated [18]. A slow thermal actuator is integrated above the ring and used to tune the device working point, that is monitored with a sensor at the drop port.

The figures of merit used to describe the performance of a MRM are i) the insertion loss (IL), defined as

$$IL = \frac{P_{in}}{P_{avg}} \tag{1}$$

where P_{in} is the input optical power and P_{avg} is the average power at the MRM output during its operation, determined by the device working point; and ii) the extinction ratio (ER), defined as

$$ER = \frac{P_1}{P_0} \tag{2}$$

where P_1 and P_0 are the transmitted power at the MRM output for a logical '1' and for a logical '0', respectively.

In order to identify the theoretical optimum point for transmission of a MRM, the transmitter penalty (TP) is also used [19], defined as

$$TP[dB] = -10\log\left(\frac{P_1 - P_0}{2P_{in}}\right) = -10\log\left(\frac{1}{IL}\cdot\frac{ER-1}{ER+1}\right) \tag{3}$$

The theoretical optimal working condition for a modulator is found when the TP is minimized. In such operating point, a good compromise between modulation efficiency and insertion loss is observed. Indeed, the minimum TP does not coincide with the point of maximum ER, because by moving closer to the MRM resonance the insertion loss increases significantly, resulting in transmission quality degradation.

A. Second derivative extraction by means of dithering signals

The proposed control strategy to stabilize the MRM operation relies on the use of the dithering technique [12], [20]: by adding a small sinusoidal oscillation to the heater dissipated power, the MRM output light is modulated around its average value. The modulation depth of the optical output is proportional to the first derivative of the device transfer function around its working point. By synchronously demodulating the signal measured by the detector at the output with a lock-in amplifier (LIA), it is then possible to recover such information and use it for control purposes. However, this approach is not suitable to implement a locking strategy targeting the point of minimum TP. Indeed, the output dithering amplitude depends both on the transfer function first-derivative and on the quantity of light in the circuit. Therefore, a locking strategy exploiting this information is power-independent only when targeting the zero of the measured dithering signal. This is not the case of the TP minimum point, that is located on the MRM slope.

For this reason, the principle of the dithering technique has been further expanded in this paper. Given the non-linearity of the ring resonator transfer function, a perfectly sinusoidal modulation of the heater power causes a non-linear oscillation of the output light signal. Indeed, if the heater power is written as $W = W_0 + W_{dith} sin(2\pi f_{dith} t)$, where W_0 is the average power and W_{dith} the amplitude of the dithering oscillation, the transfer function $H(W)$ of the MRM can be Taylor-expanded around its bias point and the optical output power can be expressed as

$$P_{OUT}(W) = P_{IN}\{H(W_0) + H'(W_0)[W_{dith}\sin(2\pi f_{dith}t)] + \\ + \frac{H''(W_0)}{2}[W_{dith}\sin(2\pi f_{dith}t)]^2 + ...\} \tag{4}$$

By limiting the Taylor expansion to the second-order term, Equation 4 can be rewritten as

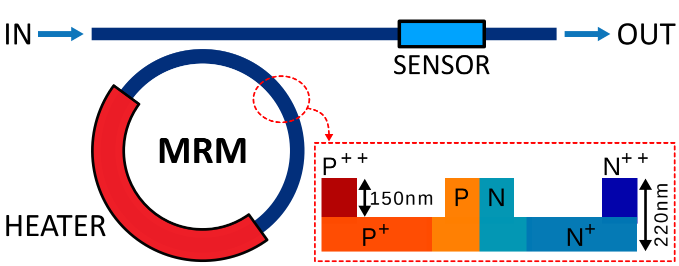

Fig. 1. Schematic view of an O-band silicon microring modulator. The heater is placed on top of the ring. In the inset, a cross-section of the waveguide is shown. The Si waveguide is partially etched to contact the pn junction with low series resistance while achieving sufficient guiding capability. For this reason, the slabs are p+ and n+ doped and the electrical contacts p++ and n++ doped.

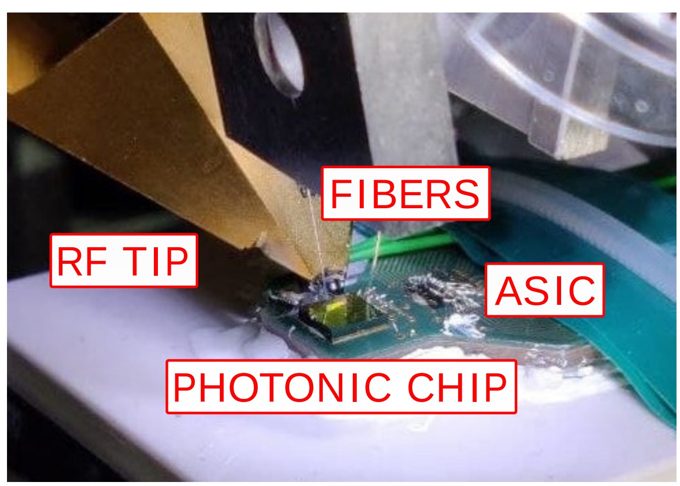

Fig. 2. Custom printed circuit board designed to house the photonic chip, the readout ASIC and allow easy optical coupling and RF access. The board is connected to a FPGA-based motherboard with all the rest of the electronics.

$$P_{OUT}(W) = P_{IN}\{H(W_0) + H'(W_0)W_{dith}\sin(2\pi f_{dith}t) + \\ + \frac{H''(W_0)}{2}W_{dith}^2[\frac{1}{2} - \frac{1}{2}\cos(2\pi 2 f_{dith}t)]\} \quad (5)$$

suggesting that, by demodulating the sensor signal at twice the heater oscillation frequency, it is possible to extract the information of the second derivative of the MRM transfer function in a specific working point. By tuning the actuator DC bias to drive the second-derivative signal to zero, it is thus possible to lock the MRM in the point of maximum slope regardless of the quantity of optical power circulating inside the chip, making the control calibration-free and robust against power fluctuations.

The considerations made so far are valid for a perfectly sinusoidal dithering power oscillation, so that the second derivative extracted from the optical output can be attributed only to the MRM transfer function non-linearity. In the case of resistive heaters driven by a current or a voltage source, this requirement is satisfied by using small dithering signals (amplitude of the dithering sinusoid much smaller than the actuator bias value) or by predistorting the actuator driving [15] to compensate for the quadratic relation between command signal and dissipated power.

III. System Description

A. Fabricated photonic chip

To assess the performance of the control strategy based on the second derivative of the MRM transfer function, the circuit in Fig. 1 was designed and fabricated in IMEC's silicon photonic ISIPP50G platform [21]. The microring resonator is an O-band all-pass ring with a radius of $7.5\,\mu\text{m}$, an FSR of $9.5\,\text{nm}$ ($1.7\,\text{THz}$), a bandwidth of $190\,\text{pm}$ ($33\,\text{GHz}$) and a Q-factor of 5000. To modulate the light, a highly-doped lateral pn junction is embedded into the ring, as shown in the cross-section in Fig. 1. The 70-nm Si slab is $10^{20}\ \text{cm}^{-3}$ p+ and n+ doped in the periphery to achieve low series resistance and improve the device bandwidth [21], while along the ring circumference a $10^{17}\ \text{cm}^{-3}$ doping is chosen to reduce the device insertion loss. To control the resonance frequency of the modulator, a tungsten integrated heater is fabricated on top of the ring at a distance of $700\,\text{nm}$ from the core, showing a resistance of about $100\,\Omega$. At the ring resonator output, a ContactLess Integrated Photonic Probe (CLIPP) [22] sensor is used to monitor the average optical power. The sensor is realized by simply depositing two metal electrodes on top of the cladding, at around $700\,\text{nm}$ from the core, to provide a capacitive access to the waveguide electrical impedance, that changes with the quantity of guided light due to sub-bandgap free-carriers generation. Two TE-polarization grating couplers (GC), each introducing $7\,\text{dB}$ of insertion loss, allow optical access with the input and output fibers.

B. Electronic system

The photonic chip was mounted on a custom interface board designed to provide easy optical coupling with the input and output fibers a nd t o a llow e lectrical a ccess with the RF tip needed to drive the modulator, as shown in Fig. 2. The photonic chip was wire-bonded to a custom ASIC for CLIPP readout [23], so to minimize the stray capacitance of the connection and maximize the sensor sensitivity. The interface board was connected to a FPGA-based multichannel motherboard with the rest of the electronics, specifically designed for photonic applications [24]. In particular, the board A/D converts (AD7903, Analog Devices) the CLIPP

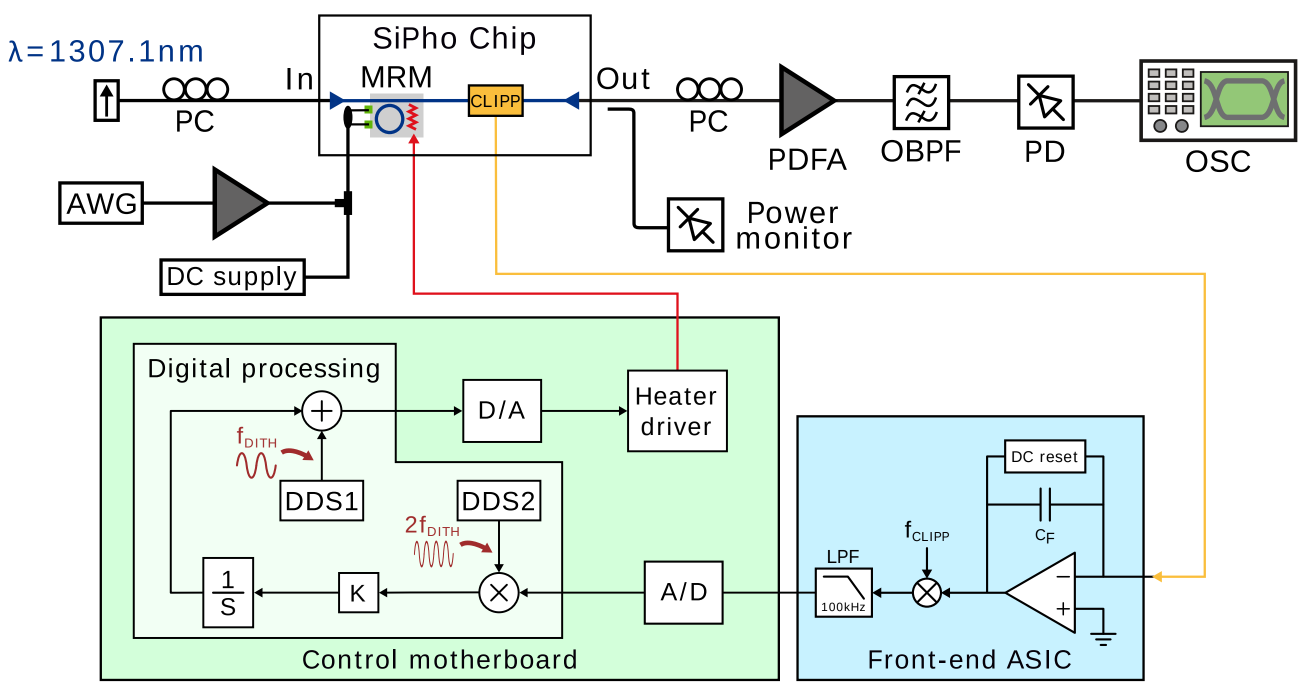

Fig. 3. Schematic view of the experimental setup used to assess the modulator and the control strategy performance.

signal and performs a digital lock-in detection, thanks to the use of a digital mixer and a tunable low-pass filter, with a bandwidth ranging from $1\,\mathrm{Hz}$ to $100\,\mathrm{kHz}$. Moreover, the board D/A converts (AD5764R, Analog Devices) the heaters signal generated by the FPGA and provides the necessary current (AD8513, Analog Devices) to drive them. The FPGA also implements the control scheme of choice to achieve real-time stabilization of the MRM. The use of an FPGA allows to create a truly parallel control scheme, so that the feedback strategy can be easily scaled to multichannel photonic systems. Without considering the FPGA, the power dissipated by the system to operate each control loop is around $40\,\mathrm{mW}$, where roughly half is dissipated by the heater and the other half is dissipated by the electronics.

C. Experimental setup

The performance of the modulator and of the control scheme were tested with the setup shown in Fig. 3. A tunable laser (TUNICS-T100S-HP) was used to generate a $0\ \mathrm{dBm}$ CW signal at $\lambda = 1307.1\ \mathrm{nm}$. An arbitrary waveform generator (AWG, MICRAM-DAC10002) was employed to create a 25 $\mathrm{Gbit/s}$ NRZ PRBS9 sequence that was sent to a high-speed amplifier (SHF-M804B) to drive the MRM with a 3 V_{PP}signal through a GS RF tip. The bias voltage of the modulator pn junction was set to $-2.5\ \mathrm{V}$ with a bias-tee. The optical signal at the output of the modulator was amplified with a PDFA, filtered with a $10\ \mathrm{nm}$ tunable bandpass filter and then measured with a photoreceiver (U^{2}t-XPVD3120R). The electrical signal was sent to a samplescope (Keysight-N1000A/N1046A) to assess the quality of the transmission. Polarization controllers (PC) were used in the setup to provide the right polarization for each component. The temperature of the chip was measured with a $10\ \mathrm{k\Omega}$ thermistor placed on the interface board next to the photonic chip, and the whole setup was kept at 28 °C with a thermo-electric cooler (TEC).

Figure 3 also shows the implemented control scheme. The dithering oscillation is a sine wave generated by the FPGA with the direct digital synthesizer (DDS) DDS1. The choice of the dithering frequency is determined by the thermal relaxation time of the heater T_h (in the order of few µs in this technology) and by the $1/f$ noise corner frequency f_C of the readout electronics (few hundreds of Hz in our case). To maximize the system performance, the condition $f_c < f_{dith} < 1/T_h$ is targeted, here satisfied by choosing $f_{dith} = 6\,\mathrm{kHz}$. The generated dithering signal is summed with a digital adder to the DC value and fed to the heater with a DAC. The optical power in the waveguide is measured with a CLIPP placed at the MRM through port. The second derivative of the transfer function is extracted with the use of a digital mixer, fed by another DDS (DDS2). By choosing the same clock for the two DDSs, the frequency generated by DDS2 is exactly equal to $2 \cdot f_{dith}$, as long as its phase increment is exactly twice the one used by DDS1. The phase of the sine wave generated by DDS2 is tuned in order to compensate for the phase shift introduced by the acquisition chain before the digital mixer. The extracted signal is finally low-pass filtered and fed to a digital integrator, that moves the heater DC power in order to drive to zero the measured dithering amplitude.

IV. Validation of the control strategy

A. MRM characterization

The described system was first used to measure the first and second derivatives of the MRM transfer function. This operation was done by linearly increasing the heater power while summing a $6\,\mathrm{kHz}$ dithering signal of around $50\,\mathrm{\mu W}$ (practically obtained with a voltage amplitude of $2\,\mathrm{mV}$) to the average value. The electronic system was set to synchronously demodulate the CLIPP readout at $6\,\mathrm{kHz}$ and $12\,\mathrm{kHz}$. The results are shown in Fig. 4. As expected, the zeroes of second derivative correspond to the stationary points of the first derivative, that in turns correspond to the points where the slope of the ring transfer function is maximum. Notice that the position of the zeroes does not depend on the quantity of light circulating inside the ring, that only affects the magnitude of the measured signals.

B. Second-Derivative MRM Locking

To assess the effectiveness of the proposed control strategy, the sole ring modulator performance was first investigated. To do so, the heater power was manually ramped while keeping the dithering oscillation disabled and the RF modulation active. The ER of the output light signal was continuously measured with the samplescope and the obtained results are shown in Fig. 5a in the trace "dith OFF". By measuring the IL with a low-speed power monitor and by using Equation 3 we computed the TP, reported in Fig. 5b. The working condition that achieves the best modulation performance is the point where the TP is minimized. In this situation, the measured output light power was $-18.9\,\mathrm{dBm}$, resulting in an estimated modulator insertion loss of $4.9\,\mathrm{dB}$. Figure 5c depicts the respective captured eye-diagram, with a Q-factor of 8.45 and an ER of $11\,\mathrm{dB}$.

To quantify the effect of the dithering signal on the transmission, the experiment was repeated by activating different

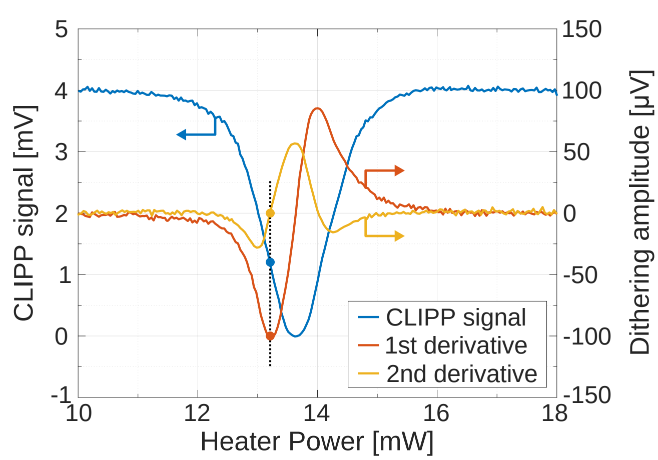

Fig. 4. Transfer function of the ring resonator (blue track) and its first (red) and second derivatives (yellow) obtained by means of the dithering technique. The measurement was obtained by sweeping the heater power and by demodulating the CLIPP signal both at the dithering frequency and at twice that frequency. As expected, the point of maximum slope of the ring transfer function corresponds to the maximum of the first derivative signal and to the zero of the second derivative.

oscillation amplitudes. Once again, the ER of the output signal was continuously measured with the samplescope and, together with the insertion losses, used to estimate the overall TP. The obtained results are shown in Fig. 5. For oscillations of the heater power of $50\,\mu\mathrm{W}$ amplitude, the ER is worsened of $1\,\mathrm{dB}$ at maximum, while negligible effects can be observed in the TP. A slightly higher degradation is instead observed in the $100\,\mu\mathrm{W}$ case, that for this reason was discarded in the following experiments.

Since the control scheme searches for the zeroes of the MRM transfer function second derivative, the device is locked in the point of its maximum slope. This point does not coincide with the TP minimum. To assess how far these two working conditions are, the locking points of the system are marked in Fig. 5(a) and 5(b). It is possible to see how these values are very close to the minimum of the TP and well within a $1\,\mathrm{dB}$ tolerance region. This leads to no measurable deterioration of the modulator performance [21], as also confirmed by the eye diagrams in Fig. 5c. The proposed technique allows to lock the MRM on both the blue and the red side of the resonance, simply by changing the sign of the acquired dithering signal to invert the behaviour of the integrator. The blue side is usually preferred, in order to avoid feedback instabilities due to self-heating effects [16], [25]–[27]. Further investigation is instead needed to understand the impact of the MRM Q-factor on the locking and modulation performance.

C. Automatic recovery from wavelength variations

The performance of the control scheme was also assessed in terms of its capability to swiftly recover from abrupt MRM working point variations. While using a dithering power of $50\,\mu\mathrm{W}$ to have minimum degradation in the transmission performance, a wavelength variation was imposed to the system. Figure 6a reports the output power measured with the external power monitor while the control feedback was active. After $130\,\mathrm{ms}$, the wavelength of the input laser was abruptly changed from $1307.6\,\mathrm{nm}$ to $1307.7\,\mathrm{nm}$ (+$100\,\mathrm{pm}$). The signal measured by the power monitor instantaneously changed from $-18\,\mathrm{dBm}$ to $-14\,\mathrm{dBm}$, due to the shift of the MRM working condition. The reaction of the control loop is demonstrated by the evolution of the heater power shown in Fig. 6b, that increases in order to compensate for the shift with a rise time of $30\,\mathrm{ms}$. The control correctly restores the initial value of the output power, proving that the system is able to recover the original working condition. The quality of the transmission is also restored, as indicated by the two eyes captured before and after the disturbance, that show no difference between each other. Being the wavelength and temperature fluctuations in real systems usually characterized by a slow evolution, often in the hundreds of milliseconds timescale, the achieved control speed is sufficient for most applications. If a faster reaction time is needed, the CLIPP sensor can be replaced by a more sensitive detector, since a higher readout signal-to-noise ratio (SNR) can be traded to obtain a larger control bandwidth, while keeping the same modulation accuracy.

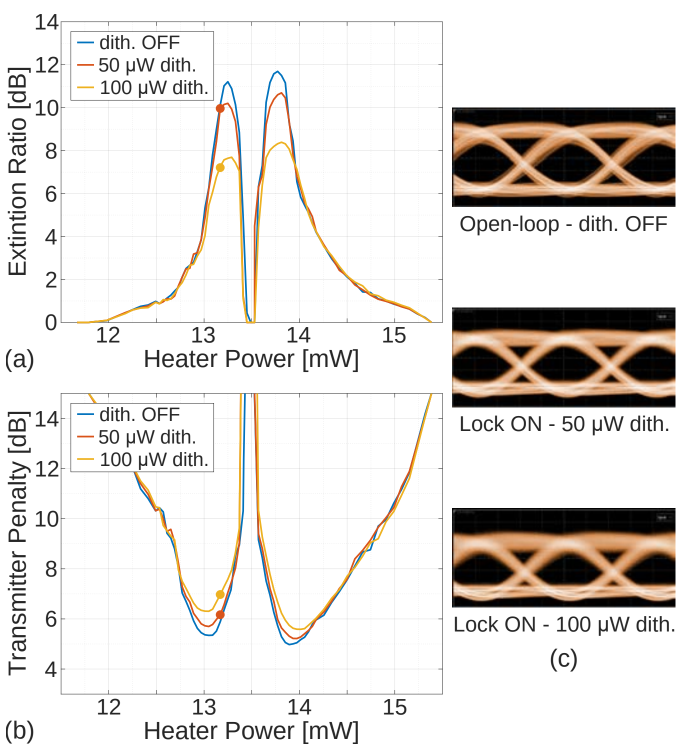

Fig. 5. (a) Extinction Ratio and (b) Transmitter Penalty measured at the MRM output. The curves are obtained for different dithering amplitudes (dithering off, $50\,\mu\mathrm{W}$ and $100\,\mu\mathrm{W}$). The circles indicate the working point targeted by the control scheme, showing that the system is able to converge to a condition very close to the TP minimum. (c) Eye diagrams measured when manually tuning the MRM in the optimum operating point, compared to those obtained when automatically locking the device with the proposed control strategy.

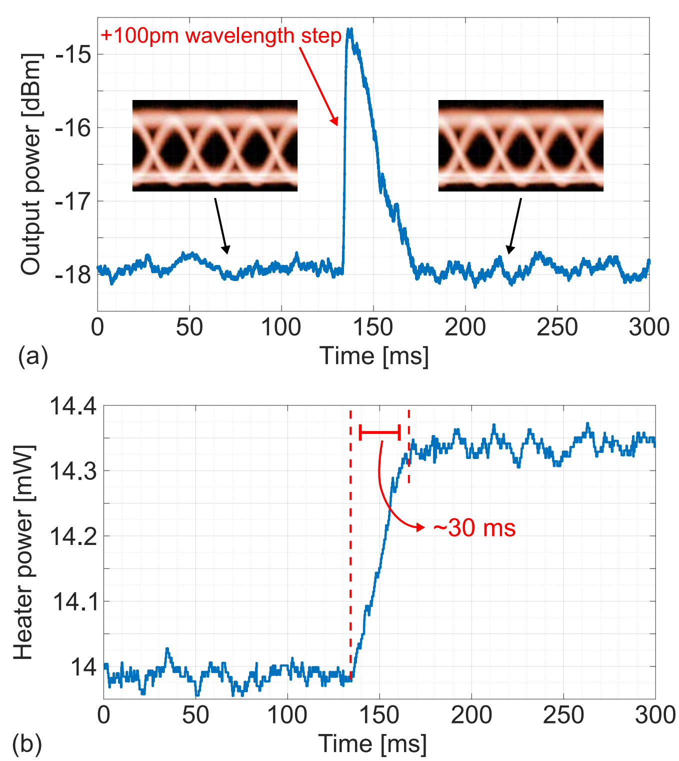

Fig. 6. Time evolution of (a) the optical power at the MRM output and (b) the heater power when abruptly changing the laser wavelength of +$100\,\mathrm{pm}$ (at $t = 130\,\mathrm{ms}$) with the feedback control loop activated. After the disturbance, the MRM working point shifts to the right, so the heater power has to increase to move the device transfer function in the same direction.

V. 50-G TRANSMISSION EXPERIMENT

The same experimental setup shown in Fig. 3 was also used to drive the MRM with a $50\,\mathrm{Gbit/s}$ on-off keying (OOK) modulation scheme. Since the control algorithm is not based on the direct assessment of the transmission performance, the modulation scheme has no effect on the locking accuracy. In the following experiments, that had a duration of around 10 minutes, one external variable was manually swept in order to simulate a slowly-varying environment.

A. Wavelength drift compensation

During a 15-minute-long experiment, the wavelength of the input laser was slowly increased from $1306\,\mathrm{nm}$ to $1314\,\mathrm{nm}$ with the control loop constantly active. The results are reported in Fig. 7. During the whole experiment, the power measured at the input of the PDFA remains constant. As shown in Fig. 7b, the heater power follows closely the laser shift, showing how the control action is able to always restore the correct working point of the modulator. The quality of the transmission, assessed by measuring the Q-factor of the output signal throughout the whole experiment, is thus not impaired. The average Q-factor value of 4.75 corresponds to a theoretical BER of 10^{-6} [28], well below the forward error correction threshold normally required for OOK transmission [29]. Figure 7 also reports three eyes taken at three different instants during the experiment, showing no measurable difference between each other.

B. Thermal drift compensation

The main challenge in employing Silicon Photonics circuits in datacenters comes from temperature fluctuations. Thus, the proposed control scheme was also tested in a temperature unstable scenario, to demonstrate that it can effectively compensate thermal drifts in real time. To this aim, temperature oscillations were intentionally generated in the setup using the TEC controller. As shown in Fig. 8, the temperature was increased from $28\,°\mathrm{C}$ to $38\,°\mathrm{C}$ during an 8-minute-long experiment. The controlled heater power mirrors perfectly the temperature profile, confirming that the control action is able to compensate any shift introduced by external perturbations. As a result, the output power measured at the input of the PDFA remains constant, apart from a negligible variation at high temperature due to a small light coupling drift in the setup. The Q-factor of the output signal, continuously assessed

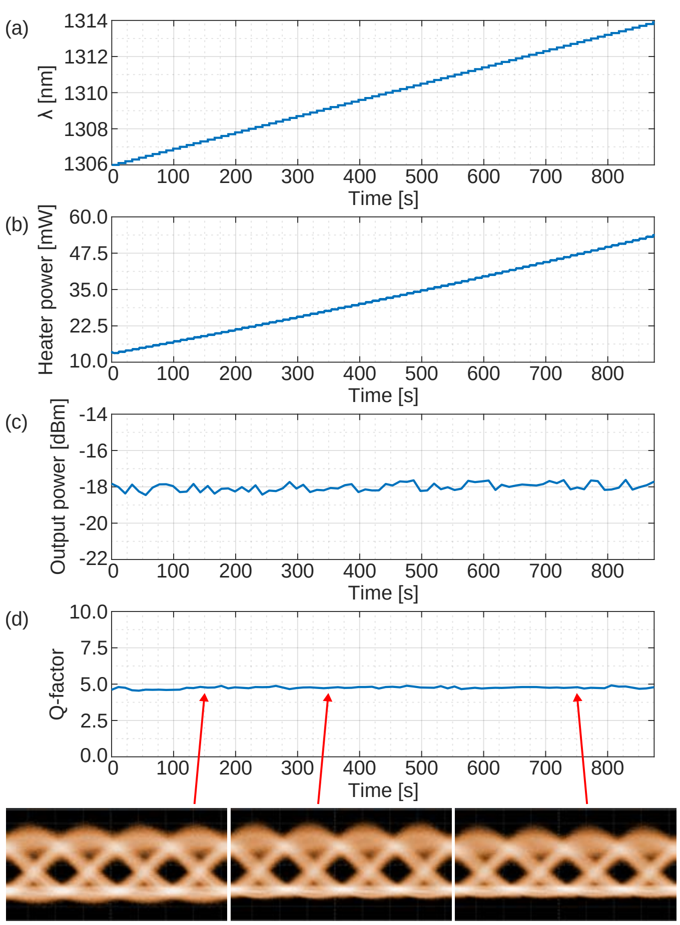

Fig. 7. Time evolution of (a) input laser wavelength, (b) heater power, (c) output optical power and (d) output eye diagram Q-factor, obtained when moving the laser wavelength from $1306\,\mathrm{nm}$ to $1314\,\mathrm{nm}$ while transmitting a $50\,\mathrm{Gbit/s}$ signal. The feedback loop updates the heater power in real-time to compensate the wavelength shift, preserving the transmission quality.

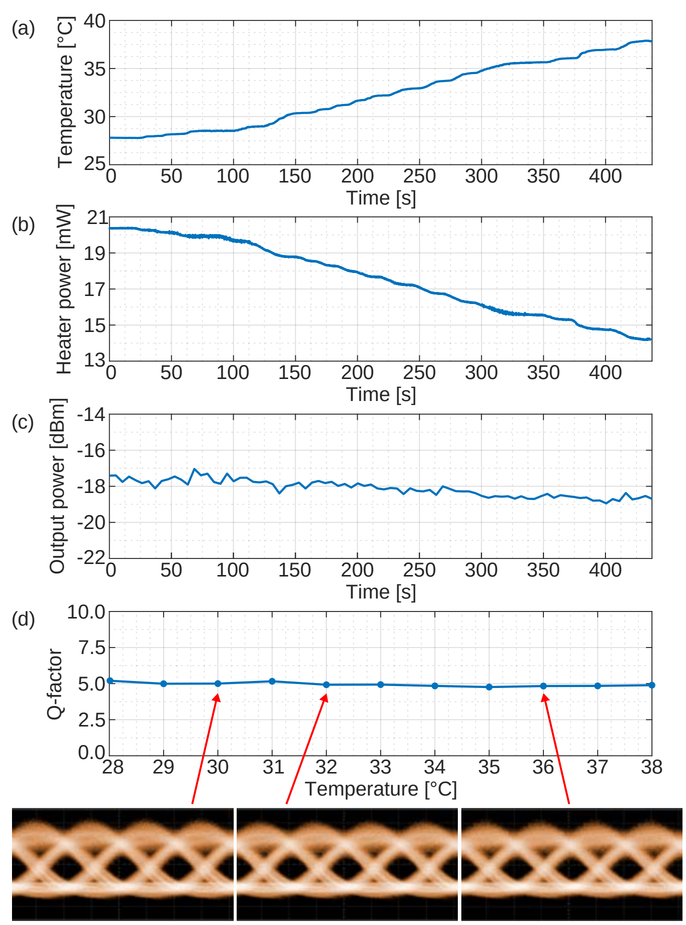

Fig. 8. (a) Chip temperature profile obtained by operating the TEC in the setup. (b) The heater power mirrors perfectly the temperature evolution to compensate any shift in the MRM transfer function. As a result, the output power (c) remains constant, apart for a minor fiber-chip misalignment, and the output eye diagram Q-factor (d) does not change with temperature.

TABLE I
COMPARISON OF STATE-OF-THE-ART CONTROL STRATEGIES FOR MRMS

	[12]	[15]	[16]	[17]	[30]	This work
Laser band	C-band	O-band	O-band	C-band	C-band	O-band
Control strategy	Output power monitoring	Input and through port power monitoring	Input power and MRM *pn* junction current monitoring	OMA monitoring	MRM *pn* junction current monitoring	MRM second-derivative extraction
Number of sensors	1 (external)	2	1 + ring *pn* junction	1	Ring *pn* junction	1
Requires calibration	Yes	Yes	Yes	No	Yes	No
Power-independent	No	Yes	Yes	Yes	No	Yes
Modulation scheme	OOK	PAM4	PAM4	OOK	OOK	OOK
Data-Rate	$10\,\mathrm{Gbit/s}$	$112\,\mathrm{Gbit/s}$	$112\,\mathrm{Gbit/s}$	$2\,\mathrm{Gbit/s}$	$12.5\,\mathrm{Gbit/s}$	$50\,\mathrm{Gbit/s}$
Requires RF electronics	No	No	No	Yes	No	No

during the whole experiment, remains constant around 4.94 regardless of the global temperature of the system. In this condition, the estimated theoretical BER is $3.8 \cdot 10^{-7}$. The quality of the transmission link is therefore preserved, as also demonstrated by the eyes captured at different temperatures reported in the bottom of Fig.8.

VI. CONCLUSIONS

The dithering technique has proven to be very effective in stabilizing the working condition of a microring modulator in the region of maximum slope of its transfer function, close to the theoretical optimum point of minimum transmitter penalty. Experiments at $50\,\mathrm{Gbit/s}$ have shown that the proposed approach allows to preserve the transmission quality even in presence of temperature and wavelength instabilities, two major issues found when operating MRM in challenging environments like datacenters. Considering that the control only requires a sensor after the modulator, the microring-heater-detector subsystem is very compact and it can therefore be effectively integrated in any optical transceiver. The possibility of achieving a calibration-free and power-independent real-time control validates the approach, as it can be seen from the comparison reported in Table I with other state-of-the-art solutions for MRMs active stabilization. Finally, the dithering technique allows to extract also the first-derivative of any device transfer function, therefore the proposed control scheme also allows to stabilize components, such as MZIs or add/drop ring resonators, in the point of minimum (or maximum) transmission [20]. The same electronic system can thus be used to fully control and stabilize heterogeneous architectures performing multiple functionalities in the same chip, opening the way to highly integrated photonic systems.

REFERENCES

[1] Cisco, “Cisco annual internet report (2018-2023) white paper,” 2020.

[2] D. A. B. Miller, “Rationale and challenges for optical interconnects to electronic chips,” *Proceedings of the IEEE*, vol. 88, no. 6, pp. 728–749, 2000.

[3] T. Alexoudi, N. Terzenidis, S. Pitris, M. Moralis-Pegios, P. Maniotis, C. Vagionas, C. Mitsolidou, G. Mourgias-Alexandris, G. T. Kanellos, A. Miliou, K. Vyrsokinos, and N. Pleros, “Optics in computing: from photonic network-on-chip to chip-to-chip interconnects and disintegrated architectures,” *Journal of Lightwave Technology*, vol. 37, no. 2, pp. 363–379, 2019.

[4] F. Zanetto, V. Grimaldi, M. Moralis-Pegios, S. Pitris, K. Fotiadis, T. Alexoudi, E. Guglielmi, D. Aguiar, P. De Heyn, Y. Ban, J. Van Campenhout, N. Pleros, G. Ferrari, M. Sampietro, and A. Melloni, “WDM-based silicon photonic multi-socket interconnect architecture with automated wavelength and thermal drift compensation,” *Journal of Lightwave Technology*, vol. 38, no. 21, pp. 6000–6006, 2020.

[5] D. A. B. Miller, “Device requirements for optical interconnects to silicon chips,” *Proceedings of the IEEE*, vol. 97, no. 7, pp. 1166–1185, 2009.

[6] M. Moralis-Pegios, S. Pitris, T. Alexoudi, N. Terzenidis, H. Ramon, J. Lambrecht, J. Bauwelinck, X. Yin, Y. Ban, P. De Heyn, J. Van Campenhout, T. Lamprecht, A. Lehnman, and N. Pleros, “4-channel 200 gb/s wdm o-band silicon photonic transceiver sub-assembly,” *Optics Express*, vol. 28, no. 4, pp. 5706–5714, 2020.

[7] R. Soref, “The past, present, and future of Silicon Photonics,” *IEEE Journal of Selected Topics in Quantum Electronics*, vol. 12, no. 6, pp. 1678–1687, 2006.

[8] D. Thomson, A. Zilkie, J. E. Bowers, T. Komljenovic, G. T. Reed, L. Vivien, D. Marris-Morini, E. Cassan, L. Virot, J.-M. Fédéli, J.-M. Hartmann, J. H. Schmid, D.-X. Xu, F. Boeuf, P. O’Brien, G. Z. Mashanovich, and M. Nedeljkovic, “Roadmap on silicon photonics,” *Journal of Optics*, vol. 18, no. 7, p. 073003, 2016.

[9] W. Bogaerts, P. De Heyn, T. Van Vaerenbergh, K. De Vos, S. Kumar Selvaraja, T. Claes, P. Dumon, P. Bienstman, D. Van Thourhout, and R. Baets, “Silicon microring resonators,” *Laser & Photonics Reviews*, vol. 6, no. 1, pp. 47–73, 2012.

[10] A. Samani, E. El-Fiky, M. Morsy-Osman, R. Li, D. Patel, T. Hoang, M. Jacques, M. Chagnon, N. Abadía, and D. V. Plant, “Silicon photonic Mach-Zehnder modulator architectures for on chip PAM-4 signal generation,” *Journal of Lightwave Technology*, vol. 37, no. 13, pp. 2989–2999, 2019.

[11] I. García López, P. Rito, D. Petousi, S. Lischke, D. Knoll, M. Kroh, L. Zimmermann, M. Ko, A. Cagri Ulusoy, and D. Kissinger, “Monolithically integrated si photonics transmitters in 0.25 μm bicmos platform for high-speed optical communications,” in *2018 IEEE/MTT-S International Microwave Symposium-IMS*, 2018, pp. 1312–1315.

[12] K. Padmaraju, J. Chan, L. Chen, M. Lipson, and K. Bergman, “Thermal stabilization of a microring modulator using feedback control,” *Optics Express*, vol. 20, no. 27, pp. 27 999–28 008, 2012.

[13] Y. Li and A. W. Poon, “Active resonance wavelength stabilization for silicon microring resonators with an in-resonator defect-state-absorption-based photodetector,” *Optics express*, vol. 23, no. 1, pp. 360–372, 2015.

[14] X. Zheng, E. Chang, P. Amberg, I. Shubin, J. Lexau, F. Liu, H. Thacker, S. S. Djordjevic, S. Lin, Y. Luo, J. Yao, J.-H. Lee, K. Raj, R. Ho, J. E. Cunningham, and A. V. Krishnamoorthy, “A high-speed, tunable silicon photonic ring modulator integrated with ultra-efficient active wavelength control,” *Optics express*, vol. 22, no. 10, pp. 12 628–12 633, 2014.

[15] H. Li, G. Balamurugan, T. Kim, M. N. Sakib, R. Kumar, H. Rong, J. Jaussi, and B. Casper, “A 3D-integrated silicon photonic microring-based 112-Gb/s PAM-4 transmitter with nonlinear equalization and thermal control,” *IEEE Journal of Solid-State Circuits*, vol. 56, no. 1, pp. 19–29, 2021.

[16] J. Sharma, Z. Xuan, H. Li, T. Kim, R. Kumar, M. N. Sakib, C.-M. Hsu, C. Ma, H. Rong, G. Balamurugan, and J. Jaussi, “Silicon photonic microring-based 4 x 112 Gb/s WDM transmitter with photocurrent-based thermal control in 28-nm CMOS,” *IEEE Journal of Solid-State Circuits*, vol. 57, no. 4, pp. 1187–1198, 2021.

[17] S. Agarwal, M. Ingels, M. Pantouvaki, M. Steyaert, P. Absil, and J. Van

Campenhout, "Wavelength locking of a Si ring modulator using an integrated drop-port OMA monitoring circuit," *IEEE Journal of Solid-State Circuits*, vol. 51, no. 10, pp. 2328–2344, 2016.

[18] R. A. Soref and B. R. Bennett, "Electrooptical effects in silicon," *IEEE journal of quantum electronics*, vol. 23, no. 1, pp. 123–129, 1987.

[19] M. Pantouvaki, P. Verheyen, G. Lepage, J. De Coster, H. Yu, P. De Heyn, P. Absil, and J. Van Campenhout, "20gb/s silicon ring modulator co-integrated with a ge monitor photodetector," in *39th European Conference and Exhibition on Optical Communication (ECOC 2013)*, 2013, pp. 1–3.

[20] F. Zanetto, V. Grimaldi, F. Toso, E. Guglielmi, M. Milanizadeh, D. Aguiar, M. Moralis-Pegios, S. Pitris, T. Alexoudi, F. Morichetti, A. Melloni, G. Ferrari, and M. Sampietro, "Dithering-based real-time control of cascaded silicon photonic devices by means of non-invasive detectors," *IET Optoelectronics*, vol. 15, no. 2, pp. 111–120, 2021.

[21] M. Pantouvaki, S. A. Srinivasan, Y. Ban, P. De Heyn, P. Verheyen, G. Lepage, H. Chen, J. De Coster, N. Golshani, S. Balakrishnan, P. Absil, and J. Van Campenhout, "Active components for 50 Gb/s NRZ-OOK optical interconnects in a Silicon Photonics platform," *Journal of Lightwave Technology*, vol. 35, no. 4, pp. 631–638, 2017.

[22] F. Morichetti, S. Grillanda, M. Carminati, G. Ferrari, M. Sampietro, M. J. Strain, M. Sorel, and A. Melloni, "Non-invasive on-chip light observation by contactless waveguide conductivity monitoring," *IEEE Journal of Selected Topics in Quantum Electronics*, vol. 20, no. 4, pp. 292–301, 2014.

[23] E. Guglielmi, F. Toso, F. Zanetto, G. Sciortino, A. Mesri, M. Sampietro, and G. Ferrari, "High-value tunable pseudo-resistors design," *IEEE Journal of Solid-State Circuits*, vol. 55, no. 8, pp. 2094–2105, 2020.

[24] E. Guglielmi, M. Carminati, F. Zanetto, A. Annoni, F. Morichetti, A. Melloni, M. Sampietro, and G. Ferrari, "16-channel modular platform for automatic control and reconfiguration of complex photonic circuits," in *2017 IEEE International Symposium on Circuits and Systems (ISCAS)*, 2017, pp. 1–4.

[25] G. Priem, P. Dumon, W. Bogaerts, D. V. Thourhout, G. Morthier, and R. Baets, "Optical bistability and pulsating behaviour in silicon-on-insulator ring resonator structures." *Opt. Express*, vol. 13, no. 23, pp. 9623–9628, Nov 2005. [Online]. Available: http://opg.optica.org/oe/abstract.cfm?URI=oe-13-23-9623

[26] C. Sun, M. Wade, M. Georgas, S. Lin, L. Alloatti, B. Moss, R. Kumar, A. H. Atabaki, F. Pavanello, J. M. Shainline, J. S. Orcutt, R. J. Ram, M. Popović, and V. Stojanović, "A 45 nm cmos-soi monolithic photonics platform with bit-statistics-based resonant microring thermal tuning," *IEEE Journal of Solid-State Circuits*, vol. 51, no. 4, pp. 893–907, 2016.

[27] M. de Cea, A. H. Atabaki, and R. J. Ram, "Power handling of silicon microring modulators," *Opt. Express*, vol. 27, no. 17, pp. 24 274–24 285, Aug 2019. [Online]. Available: http://opg.optica.org/oe/abstract.cfm?URI=oe-27-17-24274

[28] W. Freude, R. Schmogrow, B. Nebendahl, M. Winter, A. Josten, D. Hillerkuss, S. Koenig, J. Meyer, M. Dreschmann, M. Huebner, C. Koos, J. Becker, and J. Leuthold, "Quality metrics for optical signals: eye diagram, Q-factor, OSNR, EVM and BER," in *2012 14th International Conference on Transparent Optical Networks (ICTON)*, 2012, pp. 1–4.

[29] A. Udalcovs, T. Salgals, L. Zhang, X. Pang, A. Djupsjöbacka, S. Spolitis, V. Bobrovs, S. Popov, and O. Ozolins, "Optical power budget of 25+ Gbps IM/DD PON with digital signal post-equalization," *Applied Sciences*, vol. 10, no. 17, p. 6106, 2020.

[30] Z. Wang, D. Paez, A. I. A. El-Rahman, P. Wang, L. Dow, J. C. Cartledge, and A. P. Knights, "Resonance control of a silicon microring resonator modulator under high-speed operation using the intrinsic defect-mediated photocurrent," *Opt. Express*, vol. 25, no. 20, pp. 24 827–24 836, Oct 2017.